

Simulation of Higher-Order Topological Phases and Related Topological Phase Transitions in a Superconducting Qubit

Jingjing Niu,^{1,*} Tongxing Yan,^{1,*} Yuxuan Zhou,^{1,*} Ziyu Tao,¹ Xiaole Li,¹ Weiyang Liu,¹
Libo Zhang,¹ Song Liu,^{1,†} Zhongbo Yan,^{2,‡} Yuanzhen Chen,^{1,§} and Dapeng Yu¹

¹*Institute for Quantum Science and Engineering and Department of Physics,
Southern University of Science and Technology, Shenzhen 518055, China*

²*School of Physics, Sun Yat-Sen University, Guangzhou 510275, China*

Higher-order topological insulators (TIs) and superconductors (TSCs) give rise to new bulk and boundary physics, as well as new classes of topological phase transitions. While higher-order TIs have been actively studied on many platforms, the experimental study of higher-order TSCs has thus far been greatly hindered due to the scarcity of material realizations. To advance the study of higher-order TSCs, in this work we carry out the simulation of a two-dimensional spinless second-order TSC belonging to the symmetry class D in a superconducting qubit. Owing to the great flexibility and controllability of the quantum simulator, we observe the realization of higher-order topology directly through the measurement of the pseudo-spin texture in momentum space of the bulk for the first time, in sharp contrast to previous experiments based on the detection of gapless boundary modes in real space. Also through the measurement of the evolution of pseudo-spin texture with parameters, we further observe novel topological phase transitions from the second-order TSC to the trivial superconductor, as well as to the first-order TSC with nonzero Chern number. Our work sheds new light on the study of higher-order topological phases and topological phase transitions.

The bulk-boundary correspondence is a fundamental principle of topological phases of matter. Very recently, higher-order TIs and TSCs have attracted broad interest owing to their unconventional bulk-boundary correspondence [1–10]. In comparison to their conventional counterparts, also known as first-order TIs and TSCs [11, 12], the unconventionality is manifested through the codimension of their gapless boundary modes. Concretely, the boundary modes of n th order TIs or TSCs have codimension n , with $n = 1$ and $n \geq 2$ corresponding to the first-order and higher-order ones, respectively.

Two- and three-dimensional higher-order TIs have already been experimentally realized in many platforms, including photonic crystals [13–16], microwave resonators [17], electric circuits [18, 19], phononic metamaterials [20–24], and a few electronic materials [25, 26]. In sharp contrast, higher-order TSCs have so far been little explored in experiment [27], owing to the underlying difficulty in realizing this class of novel phases in real materials [28–46]. While various classical systems, like the previously mentioned electric circuits and phononic metamaterials [18–24], have played an active role in the experimental study of higher-order TIs, they generally fail to simulate higher-order TSCs as they lack the intrinsic particle-hole symmetry of superconductors. Moreover, thus far the experimental study of higher-order topological phases has been greatly restricted to the gapless boundary modes, novel physics directly related to the bulk, like topological phase transitions, has still been little explored in experiment [47]. Particularly, we notice that a novel class of topological phase transitions, which take place between higher-order and first-order topological phases within the same symmetry class, have yet to be investigated experimentally.

While the topological invariant is defined by the bulk Hamiltonian [48], the experimental detection of topological phases, both first-order and higher-order, has been greatly relying on the observation of the existence of gapless bound-

ary modes, simply because of that a direct detection of the bulk topological invariant is generally quite difficult as it requires to know the ground-state wave functions. Nevertheless, exceptions exist. When the underlying system is described by a two-by-two Hamiltonian, e.g., $H(\mathbf{k}) = \mathbf{d}(\mathbf{k}) \cdot \boldsymbol{\sigma}$ with $\boldsymbol{\sigma} = (\sigma_x, \sigma_y, \sigma_z)$ the Pauli matrices, it is known that the topological property can be simply read from the spin (or pseudo spin in general) texture in the Brillouin zone (BZ) [49–52]. One celebrated example is the Qi-Wu-Zhang model [53], which describes a quantum anomalous Hall insulator when the spin texture realizes a Skyrmion configuration.

In this work, we carry out the simulation of a two-dimensional spinless second-order TSC in a single superconducting qubit. By mapping the momentum space of the simulated two-band Bogoliubov-de Gennes (BdG) Hamiltonian to the parameter space of the qubit Hamiltonian, we are able to determine the pseudo-spin texture in the whole BZ with a combinational use of quantum-quench dynamics and quantum state tomography (QST). Through the evolution of pseudo-spin texture with parameters, we not only observe the topological phase transitions between second-order TSCs and trivial superconductors, but also observe the ones between second-order and first-order TSCs within the same symmetry class for the first time.

Theoretical model.— A spinless superconductor can be described by a two-band BdG Hamiltonian, $H = \frac{1}{2} \sum_{\mathbf{k}} \psi_{\mathbf{k}}^\dagger H_{\text{BdG}}(\mathbf{k}) \psi_{\mathbf{k}}$, with $\psi_{\mathbf{k}}^\dagger = (c_{\mathbf{k}}^\dagger, c_{-\mathbf{k}})$ and

$$H_{\text{BdG}}(\mathbf{k}) = \begin{pmatrix} \epsilon(\mathbf{k}) & \Delta(\mathbf{k}) \\ \Delta^\dagger(\mathbf{k}) & -\epsilon(\mathbf{k}) \end{pmatrix}, \quad (1)$$

where $\epsilon(\mathbf{k}) = \epsilon(-\mathbf{k})$ describes the energy of the normal state measured from the chemical potential, and $\Delta(\mathbf{k})$ is the pairing order parameter, which satisfies $\Delta(\mathbf{k}) = -\Delta(-\mathbf{k})$ due to the Fermi-Dirac statistics. The two-band form of the BdG Hamiltonian can be rewritten in terms of the Pauli matrices

σ_i ,

$$H_{\text{BdG}}(\mathbf{k}) = \sum_{i=x,y,z} d_i(\mathbf{k})\sigma_i, \quad (2)$$

with $d_x(\mathbf{k}) - id_y(\mathbf{k}) = \Delta(\mathbf{k})$, and $d_z(\mathbf{k}) = \epsilon(\mathbf{k})$. Apparently, d_x and d_y are odd under inversion, while d_z is even.

In a recent work, one of us revealed that when the three-component $\mathbf{d} = (d_x, d_y, d_z)$ vector is constructed by a Hopf map, the resulting two-band BdG Hamiltonian provides a minimal-model realization of second-order TSC [54]. Concretely, the Hopf map is $d_i(\mathbf{k}) = z^\dagger(\mathbf{k})\sigma_i z(\mathbf{k})$, where the spinor $z(\mathbf{k}) = (z_1(\mathbf{k}), z_2(\mathbf{k}))^T$, $z_1(\mathbf{k}) = f_1(\mathbf{k}) + if_2(\mathbf{k})$, and $z_2(\mathbf{k}) = g_1(\mathbf{k}) + ig_2(\mathbf{k})$, with $f_1(\mathbf{k}) = (\cos k_x + \lambda_1)$, $f_2(\mathbf{k}) = (\cos k_y + \lambda_2)$, $g_1(\mathbf{k}) = \sin k_x$, $g_2(\mathbf{k}) = \sin k_y$. Accordingly, $d_x = 2(f_1g_1 + f_2g_2)$, $d_y = 2(f_1g_2 - f_2g_1)$, and $d_z = f_1^2 + f_2^2 - g_1^2 - g_2^2$. Remarkably, this model has a simple phase diagram similar to the Benalcazar-Bernevig-Hughes model [1]. That is, when $|\lambda_{1,2}| < 1$, it realizes a second-order TSC, otherwise it describes a trivial superconductor. However, a fundamental difference lies between this model and the Benalcazar-Bernevig-Hughes model. For the latter, it belongs to either the class BDI or AI (depending on whether an on-site potential is present or not) of the Altland-Zirnbauer classification [55–57], so it cannot realize first-order topological phases. In contrast, the former belongs to the class D whose first-order topology is known to be characterized by the first Chern number [58], therefore, in principle it allows the realization of first-order TSCs, as well as topological phase transitions between second-order and first-order TSCs.

Based on the above recognition, we lift the strong constraint imposed by the Hopf map by introducing a new free parameter. For concreteness, we write down $d_{x,y,z}$ explicitly, which read

$$\begin{aligned} d_x(\mathbf{k}) &= 2\lambda_1 \sin k_x + 2\lambda_2 \sin k_y + \sin 2k_x + \sin 2k_y, \\ d_y(\mathbf{k}) &= 2\lambda_1 \sin k_y - 2\lambda_2 \sin k_x + 2 \sin(k_y - k_x), \\ d_z(\mathbf{k}) &= 2\lambda_1 \cos k_x + 2\lambda_2 \cos k_y + \cos 2k_x + \cos 2k_y - \mu, \end{aligned} \quad (3)$$

where μ denotes the chemical potential and is the free parameter. If we fix $\mu = -(\lambda_1^2 + \lambda_2^2)$, the above Hamiltonian reduces to the one in Ref. [54]. As we will show shortly, this generalized Hamiltonian has a richer phase diagram, most importantly, it allows novel topological phase transitions between second-order and first-order TSCs.

According to Eqs.(2) and (3), it is readily found that besides the particle-hole symmetry ($\mathcal{P}H_{\text{BdG}}(\mathbf{k})\mathcal{P}^{-1} = -H_{\text{BdG}}(-\mathbf{k})$ with $\mathcal{P} = \sigma_x\mathcal{K}$ and \mathcal{K} the complex conjugation), this Hamiltonian also has inversion symmetry ($\mathcal{I}H_{\text{BdG}}(\mathbf{k})\mathcal{I}^{-1} = H_{\text{BdG}}(-\mathbf{k})$ with $\mathcal{I} = \sigma_z$), which makes the determination of topological property greatly simplified. Concretely, the topological property can be simply revealed by the relative configuration between $d_z(\mathbf{k}) = 0$ (known as Fermi surface (FS) for superconductors) and $d_x(\mathbf{k}) = d_y(\mathbf{k}) = 0$ (known as Dirac pairing nodes). For the first-order topology, the parity of Chern number C is directly tied to the number of FS N_{FS} , namely $(-1)^C = (-1)^{N_{\text{FS}}}$ [59], indicating that a gapped superconductor with an odd number of FS must have nontriv-

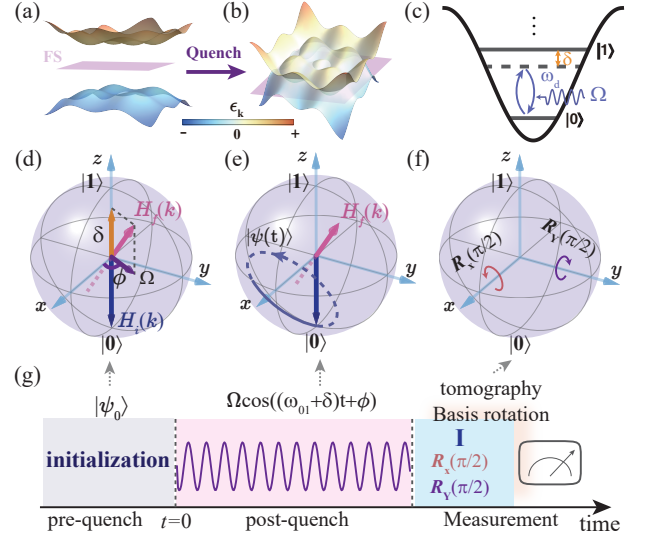


FIG. 1. Schematics of principle and experimental implementation. The energy dispersion of the normal state $\epsilon(\mathbf{k})$ for (a) pre-quench ($\lambda \rightarrow \infty$) and (b) post-quench ($\lambda = -0.5$) cases. (c) The energy diagram of an Xmon qubit. A microwave pulse is applied for simulation at each momentum via controlling its detuning frequency δ , amplitude Ω , and phase ϕ . (d) corresponds to the moment right upon the application of the quench pulse that changes the initial Hamiltonian H_i to the final Hamiltonian H_f . (e) illustrates the temporal dynamics afterwards. (f) shows rotation pulses for the QST process. (g) Time line of experimental operations.

ial first-order topology. This fact also indicates that the realization of second-order TSCs requires the number of FS to be even. Of course, only meeting this condition is not sufficient. As pointed out in Ref. [54], removable Dirac pairing nodes (not pinned at any specific momentum) is also required to be present within or between the disconnected Fermi surfaces (FSs) so that the superconductor cannot be continuously deformed to the trivial phase (no FS) without the closure of bulk gap.

Quench dynamics.— While the Hamiltonian (Eq. (2)) is simple in its form, it is not easy to be realized in an electronic material as the pairing is of p -wave nature whose material realization is rare in nature. Remarkably, the great flexibility and controllability of a superconducting qubit provides an ideal access to study this two-band BdG Hamiltonian. With this recognition, we simulate the Hamiltonian in a superconducting qubit and take advantage of the QST to determine the underlying pseudo-spin texture. Furthermore, the band topology of an equilibrium Hamiltonian can be characterized by the dynamical classification of topological quantum phases with quantum quench [60–63]. Concretely, we first prepare the qubit to stay in $|\psi_i(\mathbf{k}, t)\rangle$, the eigenstate of σ_z , i.e., $\sigma_z|\psi_i(\mathbf{k}, t)\rangle = -|\psi_i(\mathbf{k}, t)\rangle$. Such a choice corresponds to the ground state of $H_{\text{BdG}}(\mathbf{k})$ in the limit $\lambda_{1,2} \rightarrow \infty$ for which the Hamiltonian is trivial in topology (see Fig. 1(a)). Next, we suddenly quench the system at $t = 0$ by a microwave pulse

$\Omega(t) = \Omega \cos((\omega_{01} + \delta)t + \phi)$, with amplitude $\Omega = \sqrt{d_x^2 + d_y^2}$, phase $\phi = \arctan(d_y/d_x)$, and frequency detuning $\delta = d_z$ (see Fig. 1(c)(d)), then the state will follow unitary evolution, i.e., $|\psi_f(\mathbf{k}, t)\rangle = e^{iH_f(\mathbf{k})t}|\psi_i(\mathbf{k}, 0)\rangle$, where $H_f(\mathbf{k}) = \mathbf{d}(\mathbf{k}) \cdot \boldsymbol{\sigma}$ takes the form we desire to simulate.

After the quench, the pseudo-spin polarization, defined as $\mathbf{P}(\mathbf{k}, t) = \langle \psi_f(\mathbf{k}, t) | \boldsymbol{\sigma} | \psi_f(\mathbf{k}, t) \rangle$, will precess on the Bloch sphere (see illustration in Fig. 1) around the direction of $\mathbf{d}(\mathbf{k})$. In experiment, the evolution of $\mathbf{P}(\mathbf{k}, t)$ can be measured by QST. Interestingly, it was shown in Ref. [60] that the time-averaged pseudo-spin polarization is directly related to $\mathbf{d}(\mathbf{k})$. To obtain this quantity, here we flatten the Hamiltonian as $H_f(\mathbf{k})/E_f(\mathbf{k})$ with $E_f(\mathbf{k})$ the eigenenergy of $H_f(\mathbf{k})$ (such a procedure does not change the underlying topological properties), so that the time of evolution is identical for each k [63, 64]. By doing so, we find that only two periods are sufficient to obtain a trustworthy value of the time-averaged pseudo-spin polarization (see Supplemental Material (SM) for a detailed discussion). The result reads

$$P_i(\mathbf{k}) = -\frac{d_i(\mathbf{k})d_z(\mathbf{k})}{d_x^2(\mathbf{k}) + d_y^2(\mathbf{k}) + d_z^2(\mathbf{k})}, \quad (4)$$

where P_i with $i = x, y, z$ represent the three components (as shown in Fig. 1(d-f)). It is immediately seen that the FS determined by $d_z = 0$ corresponds to $P_z = 0$, and the Dirac pairing nodes determined by $d_x = d_y = 0$ can be extracted from $P_x = P_y = 0$ after the contour $P_z = 0$ is determined.

Topological phase transitions between second-order TSCs and trivial superconductors.— Our experiments were performed using Xmon type of superconducting qubits (see SM for details of samples and experimental setup). We first show the experimental results for the case with μ fixed to $-(\lambda_1^2 + \lambda_2^2)$, accordingly, the phase diagram of the simulated Hamiltonian contains only two distinct phases, a second-order TSC and a trivial superconductor [54]. Let us focus on some specific points in the parameter space at first. As shown in Fig. 2(a), when we set $\lambda_1 = \lambda_2 = \lambda = -0.5$, there are two disconnected contours that satisfy $P_z = 0$, indicating the presence of two disconnected FSs in the BZ. Figure 2(b) shows the corresponding texture of (P_x, P_y) . It is readily seen that there are four vortices and four antivortices in the BZ whose cores correspond to $P_x = P_y = 0$, with half of them located at time-reversal invariant momenta, and the other half located at some generic momenta between the two contours for $P_z = 0$. As discussed above, these vortices and antivortices refer to the Dirac pairing nodes, and the four at generic momenta represent the removable ones which are crucial for the realization of the second-order TSC [54]. By fixing $\lambda_2 = -0.5$ and decreasing λ_1 , we find that the removable vortices and antivortices move toward each other in pair and then annihilate on the $k_x = 0$ line when λ_1 reaches the critical value $\lambda_1 = -1$, as shown in Fig. 2(c)-(g). After the annihilation, the two contours for $P_z = 0$ can continuously move together and then annihilate without crossing any other vortices, indicating that the annihilation of removable vortices and antivortices corre-

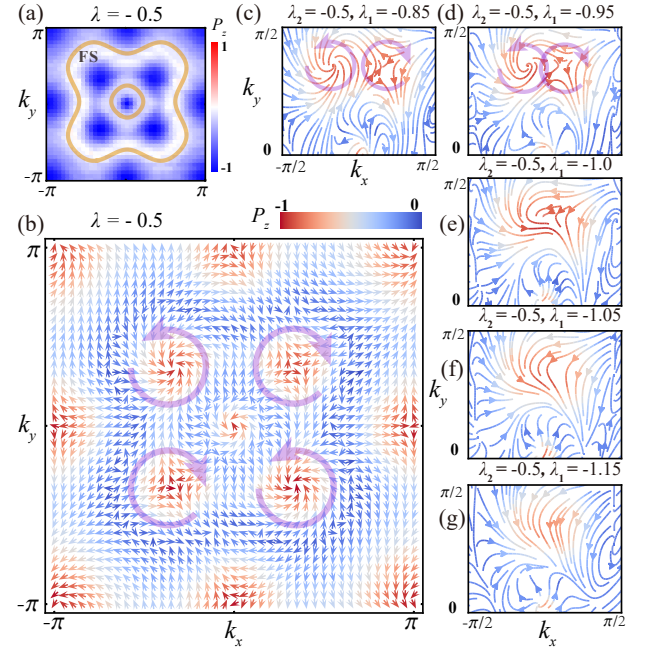


FIG. 2. Experiments demonstrating a second-order TSC and the movement and annihilation of (anti)vortices. (a) P_z measured across the BZ for a particular realization of the second-order TSC ($\lambda = -0.5$). The two closed curves indicate the FS in the first BZ where $P_z = 0$. (b) (P_x, P_y) measured across the BZ for the same realization, shown as two dimensional vectors. For completeness, P_z is also indicated using the same color bar as in (a). The circular arrows mark the four removable vortices and antivortices. (c)-(g) The movement, merging, and annihilation of a pair of vortex and antivortex manifested by evolution of the pseudo-spin texture (P_x, P_y) for $\lambda_2 = -0.5$, $\lambda_1 = -1 + \delta$, with $\delta \in [0.15, 0.05, 0, -0.05, -0.15]$.

sponds to a topological phase transition from the second-order TSC to the trivial superconductor.

To further confirm the topological phase transition, we tune the parameter to satisfy $\lambda_1 = \lambda_2 = \lambda$. Accordingly, the simulated Hamiltonian is expected to have chiral symmetry on the two lines $k_x = \pm k_y$, and its topological property can be fully characterized by the winding number defined on these two high symmetry lines [54]. As the winding number defined on them are equal, here we focus on the line $k_x = k_y$, where the winding number is given by

$$\mathcal{W}_n = \frac{1}{2\pi} \int_{-\pi}^{\pi} \frac{d_z \partial_k d_x - d_x \partial_k d_z}{d_x^2 + d_z^2} dk. \quad (5)$$

Figure 3 shows the results along the $k_x = k_y = k$ line (see SM for the $k_x = -k_y$ case). According to the observed (P_x, P_z) presented in Fig. 2(a) and (b), we successfully extract the dependence of (d_x, d_z) , and so the winding number, on λ , as shown in Fig. 3(c). Geometrically, the winding number corresponds to the number of cycles that the vector (d_x, d_z) winds around the origin ($d_x = 0, d_z = 0$) when k varies from $-\pi$ to π [65]. As the vector (d_x, d_z) is found to wind the origin twice when $|\lambda| < 1$, the geometric interpretation suggests

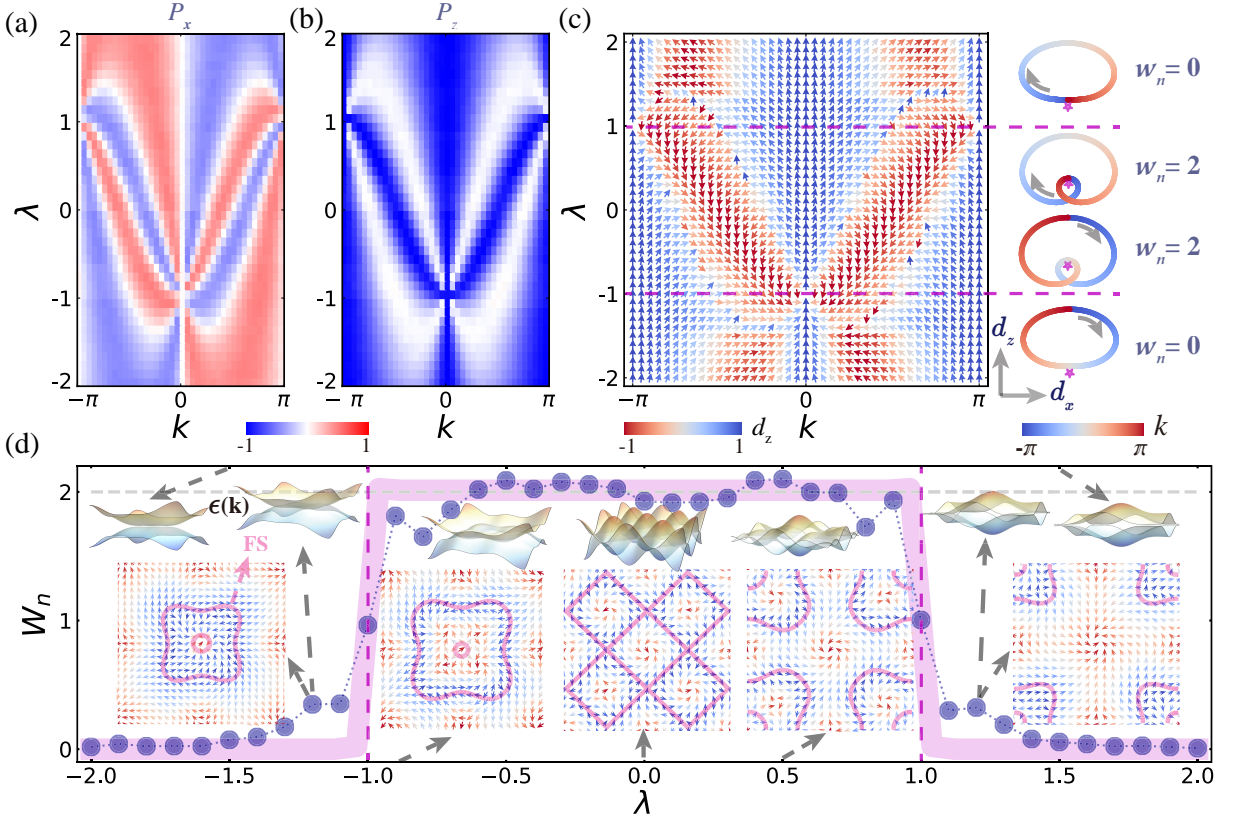


FIG. 3. Phase transition from second-order TSC to a trivial superconductor. (a) and (b) are the time-averaged spin polarizations, P_x and P_z , measured along the $k_x = k_y$ line as $\lambda_1 = \lambda_2 = \lambda$ changes continually from -2 to 2 . (c) Left: (d_x, d_z) versus k for different λ deduced from data in (a) and (b). On the right side the winding configuration of (d_x, d_z) around the origin (the stars) is shown, and the corresponding winding number \mathcal{W}_n is indicated. (d) λ -dependence of \mathcal{W}_n obtained experimentally using Eq. (5) (blue circles) and the theoretical expectation (pink line). The insets show the normal state energy dispersion $\epsilon(\mathbf{k})$, pseudo-spin texture (P_x, P_z) , as well as the FS ($P_z = 0$), for different phases.

$\mathcal{W}_n = 2$; in contrast, when $|\lambda| > 1$, no complete cycle is observed when k traverses across the BZ, suggesting $\mathcal{W}_n = 0$, as depicted on the right side of Fig. 3(c). We have also calculated the winding number by following Eq. (5) and using the experimentally obtained values of d_x and d_z , with the results presented in Fig. 3(d) (the blue circles). It is readily seen that the experimental results, while displaying certain fluctuations due to the finite discretization of the BZ, are overall in good agreement with the theoretical expectation (the pink line). In Fig. 3(d), we also present the evolution of (P_x, P_y) and the contours for $P_z = 0$. As here we set $\lambda_1 = \lambda_2 = \lambda$, one can see that the four removable vortices and antivortices of (P_x, P_y) move in a symmetrically all-inward or all-outward way with the variation of λ and the change of winding number, or say topological phase transition, is exactly associated with the annihilation of them at the time-reversal invariant momentum, $(0, 0)$ for $\lambda = -1$ and (π, π) for $\lambda = 1$.

Topological phase transitions between second-order and first-order TSCs.— When the chemical potential μ becomes variable, the number of FSs is no longer limited to be even, as a result, first-order TSC phases become possible [59]. For

the situation with $\lambda_1 = \lambda_2 = \lambda$, the phase diagram of the simulated Hamiltonian is presented in Fig. 4(a). The first-order TSC in the phase diagram has Chern number $C = 1$ as it has only one FS within which the numbers of vortices and antivortices differ by one. Before proceeding, we emphasize that the topological phase transitions between second-order and first-order TSCs and the ones between second-order TSCs and trivial superconductors display fundamental difference. As shown in Fig. 2, the latter can be achieved by simply annihilating the removable vortices and antivortices, which does not need the closure of bulk gap. In sharp contrast, the closure of bulk gap is inevitably associated with the former as they involve the change of first-order topology.

It is readily seen from Fig. 4(a) that the desired topological phase transitions between second-order and first-order TSCs can be achieved by appropriately varying λ or μ . Without loss of generality, we fix $\lambda = -0.5$ and vary μ in a broad regime (see the blue dashed line in Fig. 4(a)). Accordingly, the configuration of vortices and antivortices is expected to be intact and only the FS will change. As here the first-order TSC with $C = 1$ has a corresponding $\mathcal{W}_n = 1$, in the experiment we

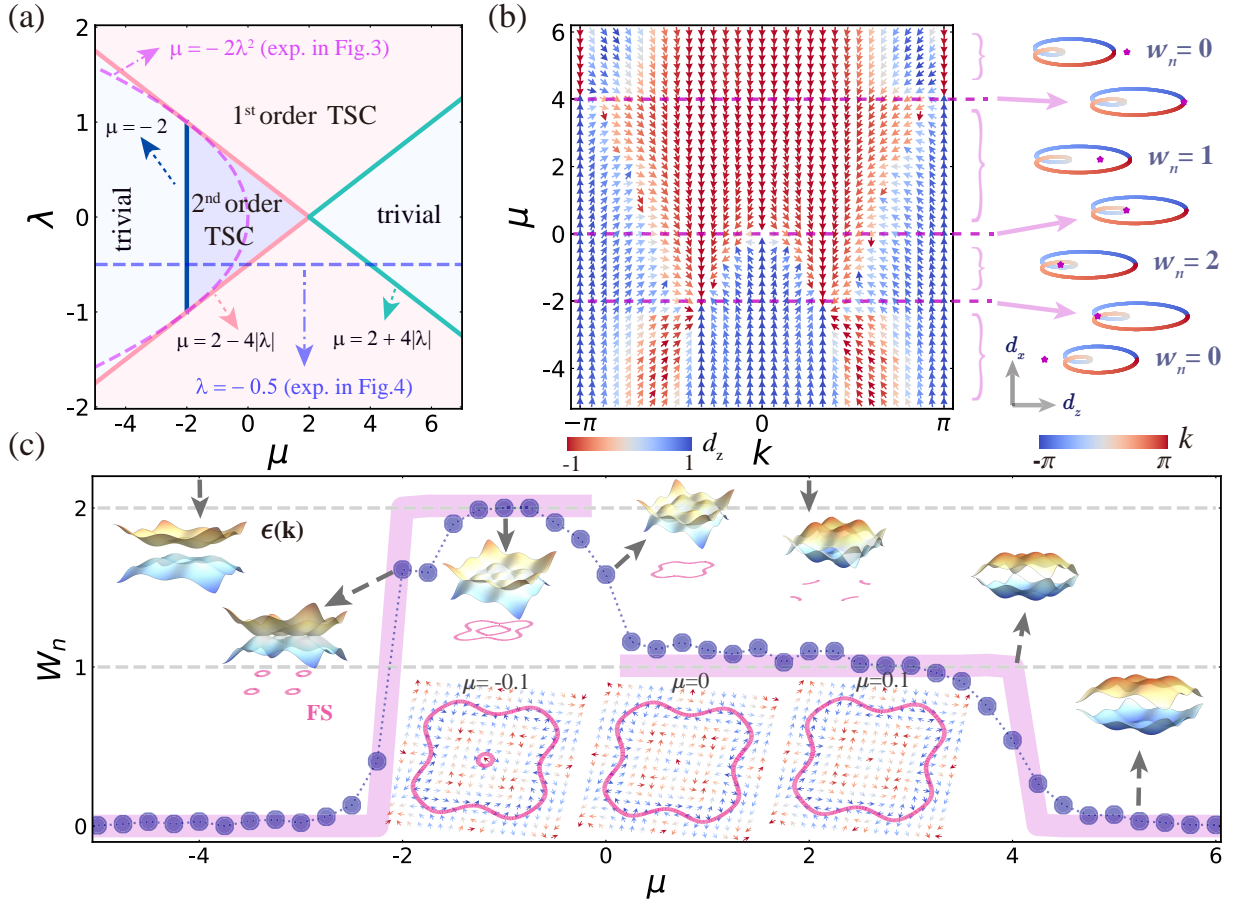


FIG. 4. Phase transitions between first- and second-order TSCs and trivial superconductors. (a) Phase diagram of the simulated Hamiltonian with $\lambda_1 = \lambda_2 = \lambda$. The blue dashed line is for $\lambda = -0.5$, which is experimentally demonstrated in (c), while the pink curve represents the experiment in Fig. 3. (b) (d_x, d_z) measured along the $k_x = k_y = k$ line for different μ with λ fixed to -0.5 . The right side shows the corresponding winding configurations (d_z, d_x) . (c) μ -dependence of W_n obtained experimentally using Eq. (5) (blue circles) and the theoretical expectation (pink line). The insets show the normal state energy dispersion $\epsilon(k)$, pseudo-spin texture (P_x, P_y) , as well as the FSs for different phases.

keep using the observed pseudo-spin texture on the $k_x = k_y$ line to extract the topological invariants, as well as the topological phase transitions.

Figure 4(b) shows the pseudo-spin texture of (d_x, d_z) on the $k_x = k_y$ line extracted from the observed (P_x, P_z) . Also according to the number of cycles that the vector (d_x, d_z) winds around the origin, we find $W_n = 2$ for $-2 < \mu < 0$ (second-order TSC), $W_n = 1$ for $0 < \mu < 4$ (first-order TSC), and $W_n = 0$ otherwise (trivial superconductor). In Fig. 4(c), the W_n deduced experimentally using Eq. (5) (the blue circles) is presented. It is readily seen that the experimentally obtained topological invariants are also in good agreement with the theoretical expectation (the pink line). For the sake of completeness, we also show the pseudo-spin texture near the critical point ($\mu = 0$) of the topological phase transition between the second-order and first-order TSCs in Fig. 4(c). One can see from the insets of Fig. 4(c) that when $\mu = -0.1$, $P_z = 0$ has two disconnected contours; at the critical point $\mu = 0$, the

smaller one contour shrinks to a point and coincides with the time-reversal invariant momentum $(0, 0)$, which leads to the closure of bulk gap; when $\mu = 0.1$, the smaller one contour completely disappears and only the larger one remains. Both the evolution of pseudo-spin texture and the change of topological invariant on the high symmetry line confirm the realization of topological phase transitions between second-order and first-order TSCs.

Discussions and Conclusions.— In summary, we have simulated a second-order topological superconducting phase in a controllable superconducting qubit and observed novel topological phase transitions between this phase and a trivial superconductor, as well as the first-order TSC within the same symmetry class. Our work opens new opportunities for the experimental study of higher-order topological phases. A direction forward is to investigate the interaction effects and the nonequilibrium properties of quenched or driven higher-order topological phases.

This work was supported by the Key-Area Research and Development Program of Guangdong Province (Grant No. 2018B030326001), the National Natural Science Foundation of China (U1801661), the National Science Foundation of China (No.11904417), the Guangdong Innovative and Entrepreneurial Research Team Program (2016ZT06D348), the Natural Science Foundation of Guangdong Province (2017B030308003), and the Science, Technology and Innovation Commission of Shenzhen Municipality (ZDSYS20170303165926217, JCYJ20170412152620376, KYTDPT20181011104202253).

* These authors contributed equally to this work.

† lius3@sustech.edu.cn

‡ yanzhb5@mail.sysu.edu.cn

§ chenyz@sustech.edu.cn

- [1] W. A. Benalcazar, B. A. Bernevig, and T. L. Hughes, *Phys. Rev. B* **96**, 245115 (2017).
- [2] F. Schindler, A. M. Cook, M. G. Vergniory, Z. Wang, S. S. Parkin, B. A. Bernevig, and T. Neupert, *Science advances* **4**, eaat0346 (2018).
- [3] Z. Song, Z. Fang, and C. Fang, *Phys. Rev. Lett.* **119**, 246402 (2017).
- [4] J. Langbehn, Y. Peng, L. Trifunovic, F. von Oppen, and P. W. Brouwer, *Phys. Rev. Lett.* **119**, 246401 (2017).
- [5] W. A. Benalcazar, B. A. Bernevig, and T. L. Hughes, *Science* **357**, 61 (2017).
- [6] M. Ezawa, *Phys. Rev. Lett.* **120**, 026801 (2018).
- [7] E. Khalaf, *Phys. Rev. B* **97**, 205136 (2018).
- [8] M. Geier, L. Trifunovic, M. Hoskam, and P. W. Brouwer, *Phys. Rev. B* **97**, 205135 (2018).
- [9] S. Franca, J. van den Brink, and I. C. Fulga, *Phys. Rev. B* **98**, 201114 (2018).
- [10] L. Trifunovic and P. W. Brouwer, *Phys. Rev. X* **9**, 011012 (2019).
- [11] M. Z. Hasan and C. L. Kane, *Rev. Mod. Phys.* **82**, 3045 (2010).
- [12] X.-L. Qi and S.-C. Zhang, *Rev. Mod. Phys.* **83**, 1057 (2011).
- [13] J. Noh, W. A. Benalcazar, S. Huang, M. J. Collins, K. P. Chen, T. L. Hughes, and M. C. Rechtsman, *Nature Photonics* **12**, 408 (2018).
- [14] X.-D. Chen, W.-M. Deng, F.-L. Shi, F.-L. Zhao, M. Chen, and J.-W. Dong, *Phys. Rev. Lett.* **122**, 233902 (2019).
- [15] B.-Y. Xie, G.-X. Su, H.-F. Wang, H. Su, X.-P. Shen, P. Zhan, M.-H. Lu, Z.-L. Wang, and Y.-F. Chen, *Phys. Rev. Lett.* **122**, 233903 (2019).
- [16] A. El Hassan, F. K. Kunst, A. Moritz, G. Andler, E. J. Bergholtz, and M. Bourennane, *Nature Photonics*, **1** (2019).
- [17] C. W. Peterson, W. A. Benalcazar, T. L. Hughes, and G. Bahl, *Nature* **555**, 346 (2018).
- [18] S. Imhof, C. Berger, F. Bayer, J. Brehm, L. W. Molenkamp, T. Kiessling, F. Schindler, C. H. Lee, M. Greiter, T. Neupert, *et al.*, *Nature Physics* **14**, 925 (2018).
- [19] J. Bao, D. Zou, W. Zhang, W. He, H. Sun, and X. Zhang, arXiv e-prints, arXiv:1911.05287 (2019), arXiv:1911.05287 [cond-mat.mes-hall].
- [20] M. Serra-Garcia, V. Peri, R. Süssstrunk, O. R. Bilal, T. Larsen, L. G. Villanueva, and S. D. Huber, *Nature* **555**, 342 (2018).
- [21] H. Xue, Y. Yang, F. Gao, Y. Chong, and B. Zhang, *Nature materials* **18**, 108 (2019).
- [22] X. Zhang, H.-X. Wang, Z.-K. Lin, Y. Tian, B. Xie, M.-H. Lu, Y.-F. Chen, and J.-H. Jiang, *Nature Physics*, **1** (2019).
- [23] H. Xue, Y. Ge, H.-X. Sun, Q. Wang, D. Jia, Y.-J. Guan, S.-Q. Yuan, Y. Chong, and B. Zhang, arXiv e-prints, arXiv:1911.06068 (2019), arXiv:1911.06068 [cond-mat.mes-hall].
- [24] X. Ni, M. Li, M. Weiner, A. Alù, and A. B. Khanikaev, arXiv e-prints, arXiv:1911.06469 (2019), arXiv:1911.06469 [cond-mat.mes-hall].
- [25] F. Schindler, Z. Wang, M. G. Vergniory, A. M. Cook, A. Murani, S. Sengupta, A. Y. Kasumov, R. Deblock, S. Jeon, I. Drozdov, *et al.*, *Nature physics* **14**, 918 (2018).
- [26] S. N. Kempkes, M. R. Slot, J. J. van den Broeke, P. Capiod, W. A. Benalcazar, D. Vanmaekelbergh, D. Bercioux, I. Swart, and C. Morais Smith, *Nature Materials* **18**, 1292 (2019).
- [27] M. J. Gray, J. Freudenstein, S. Y. F. Zhao, R. O'Connor, S. Jenkins, N. Kumar, M. Hoek, A. Kopec, S. Huh, T. Taniguchi, K. Watanabe, R. Zhong, C. Kim, G. D. Gu, and K. S. Burch, *Nano Letters* **19**, 4890 (2019).
- [28] X. Zhu, *Phys. Rev. B* **97**, 205134 (2018).
- [29] Z. Yan, F. Song, and Z. Wang, *Phys. Rev. Lett.* **121**, 096803 (2018).
- [30] Y. Wang, M. Lin, and T. L. Hughes, *Phys. Rev. B* **98**, 165144 (2018).
- [31] Q. Wang, C.-C. Liu, Y.-M. Lu, and F. Zhang, *Phys. Rev. Lett.* **121**, 186801 (2018).
- [32] T. Liu, J. J. He, and F. Nori, *Phys. Rev. B* **98**, 245413 (2018).
- [33] C.-H. Hsu, P. Stano, J. Klinovaja, and D. Loss, *Phys. Rev. Lett.* **121**, 196801 (2018).
- [34] Z. Wu, Z. Yan, and W. Huang, *Phys. Rev. B* **99**, 020508 (2019).
- [35] R.-X. Zhang, W. S. Cole, and S. Das Sarma, *Phys. Rev. Lett.* **122**, 187001 (2019).
- [36] Y. Volpez, D. Loss, and J. Klinovaja, *Phys. Rev. Lett.* **122**, 126402 (2019).
- [37] X. Zhu, *Phys. Rev. Lett.* **122**, 236401 (2019).
- [38] S. Franca, D. V. Efremov, and I. C. Fulga, *Phys. Rev. B* **100**, 075415 (2019).
- [39] Y. Peng and Y. Xu, *Phys. Rev. B* **99**, 195431 (2019).
- [40] S. A. A. Ghorashi, X. Hu, T. L. Hughes, and E. Rossi, *Phys. Rev. B* **100**, 020509 (2019).
- [41] X.-H. Pan, K.-J. Yang, L. Chen, G. Xu, C.-X. Liu, and X. Liu, *Phys. Rev. Lett.* **123**, 156801 (2019).
- [42] R.-X. Zhang, W. S. Cole, X. Wu, and S. Das Sarma, *Phys. Rev. Lett.* **123**, 167001 (2019).
- [43] Z. Yan, *Phys. Rev. B* **100**, 205406 (2019).
- [44] X. Wu, X. Liu, R. Thomale, and C.-X. Liu, arXiv e-prints, arXiv:1905.10648 (2019), arXiv:1905.10648 [cond-mat.supr-con].
- [45] Y.-T. Hsu, W. S. Cole, R.-X. Zhang, and J. D. Sau, arXiv e-prints, arXiv:1904.06361 (2019), arXiv:1904.06361 [cond-mat.supr-con].
- [46] Y.-J. Wu, J. Hou, Y.-M. Li, X.-W. Luo, and C. Zhang, arXiv e-prints, arXiv:1905.08896 (2019), arXiv:1905.08896 [cond-mat.mes-hall].
- [47] M. Serra-Garcia, R. Süssstrunk, and S. D. Huber, *Phys. Rev. B* **99**, 020304 (2019).
- [48] C.-K. Chiu, J. C. Y. Teo, A. P. Schnyder, and S. Ryu, *Rev. Mod. Phys.* **88**, 035005 (2016).
- [49] P. Roushan, C. Neill, Y. Chen, M. Kolodrubetz, C. Quintana, N. Leung, M. Fang, R. Barends, B. Campbell, Z. Chen, B. Chiaro, A. Dunsworth, E. Jeffrey, J. Kelly, A. Megrant, J. Mutus, P. J. J. O'Malley, D. Sank, A. Vainsencher, J. Wenner, T. White, A. Polkovnikov, A. N. Cleland, and J. M. Martinis, *Nature* **515**, 241 (2014).

- [50] M. D. Schroer, M. H. Kolodrubetz, W. F. Kindel, M. Sandberg, J. Gao, M. R. Vissers, D. P. Pappas, A. Polkovnikov, and K. W. Lehnert, *Phys. Rev. Lett.* **113**, 050402 (2014).
- [51] E. Flurin, V. V. Ramasesh, S. Hacoen-Gourgy, L. S. Martin, N. Y. Yao, and I. Siddiqi, *Phys. Rev. X* **7**, 031023 (2017).
- [52] X.-Y. Xu, Q.-Q. Wang, W.-W. Pan, K. Sun, J.-S. Xu, G. Chen, J.-S. Tang, M. Gong, Y.-J. Han, C.-F. Li, and G.-C. Guo, *Phys. Rev. Lett.* **120**, 260501 (2018).
- [53] X.-L. Qi, Y.-S. Wu, and S.-C. Zhang, *Phys. Rev. B* **74**, 085308 (2006).
- [54] Z. Yan, *Phys. Rev. Lett.* **123**, 177001 (2019).
- [55] A. P. Schnyder, S. Ryu, A. Furusaki, and A. W. W. Ludwig, *Phys. Rev. B* **78**, 195125 (2008).
- [56] A. Kitaev, *AIP Conference Proceedings* **1134**, 22 (2009).
- [57] S. Ryu, A. P. Schnyder, A. Furusaki, and A. W. W. Ludwig, *New Journal of Physics* **12**, 065010 (2010).
- [58] X.-L. Qi, T. L. Hughes, and S.-C. Zhang, *Phys. Rev. B* **82**, 184516 (2010).
- [59] M. Sato, *Phys. Rev. B* **81**, 220504 (2010).
- [60] L. Zhang, L. Zhang, S. Niu, and X.-J. Liu, *Science Bulletin* **63**, 1385 (2018).
- [61] W. Sun, C.-R. Yi, B.-Z. Wang, W.-W. Zhang, B. C. Sanders, X.-T. Xu, Z.-Y. Wang, J. Schmiedmayer, Y. Deng, X.-J. Liu, S. Chen, and J.-W. Pan, *Phys. Rev. Lett.* **121**, 250403 (2018).
- [62] L. Zhang, L. Zhang, and X.-J. Liu, *Phys. Rev. A* **100**, 063624 (2019).
- [63] H. Hu and E. Zhao, arXiv e-prints (2019), 1911.02211 [cond-mat.mes-hall].
- [64] X.-Y. Guo, C. Yang, Y. Zeng, Y. Peng, H.-K. Li, H. Deng, Y.-R. Jin, S. Chen, D. Zheng, and H. Fan, *Phys. Rev. Applied* **11**, 044080 (2019).
- [65] S. Ryu and Y. Hatsugai, *Phys. Rev. Lett.* **89**, 077002 (2002).

SUPPLEMENTAL MATERIAL

This supplemental material contains the following sections: (I) The derivation of the formula for time-averaged pseudo-spin polarization; (II) The determination of phase diagram; (III) Pseudo-spin polarization determined in experiment; (IV) Removable Dirac pairing nodes and topological phase transitions between second-order topological superconductors (TSCs) and trivial superconductors; (V) The change of pseudo-spin texture across topological phase transitions; (VI) Information of samples and experimental setup.

I. TIME-AVERAGED PSEUDO-SPIN POLARIZATION

In the experiment, we start with the trivial ground state $|\psi(\mathbf{k}, t)\rangle$ corresponding to the limiting situation $\lambda_{1,2} \rightarrow \infty$. That is, $|\psi(\mathbf{k}, t)\rangle$ is an eigenstate of σ_z , i.e., $\sigma_z|\psi(\mathbf{k}, t)\rangle = -|\psi(\mathbf{k}, t)\rangle$. At a time (we take it as the reference time $t = 0$), we suddenly quench the system by a microwave pulse, then the state will follow unitary evolution, with

$$|\psi_f(\mathbf{k}, t)\rangle = \mathcal{T} e^{-i \int_0^t H_f(\mathbf{k}) dt} |\psi(\mathbf{k}, 0)\rangle, \quad (\text{S1})$$

where \mathcal{T} stands for time-ordering operator and $H_f(\mathbf{k}) = \mathbf{d}(\mathbf{k}) \cdot \boldsymbol{\sigma}$ takes the form to simulate.

After the quench, the pseudo-spin polarization, which is defined as $\mathbf{P}(\mathbf{k}, t) = \langle \psi_f(\mathbf{k}, t) | \boldsymbol{\sigma} | \psi_f(\mathbf{k}, t) \rangle$, evolves with time. Below we show when the spectra of $H_f(\mathbf{k})$ are flattened, that is $H_f(\mathbf{k}) \rightarrow \bar{H}(\mathbf{k}) = H_f(\mathbf{k})/E_f(\mathbf{k})$, where $E_f(\mathbf{k}) = d(\mathbf{k}) = \sqrt{d_x^2(\mathbf{k}) + d_y^2(\mathbf{k}) + d_z^2(\mathbf{k})}$, the pseudo-spin polarization becomes time periodic and its average value over one period has a simple relation with the \mathbf{d} vector.

For the flattened Hamiltonian, we have

$$\begin{aligned} |\psi_f(\mathbf{k}, t)\rangle &= \mathcal{T} e^{-i \int_0^t \bar{H}(\mathbf{k}) dt} |\psi(\mathbf{k}, 0)\rangle \\ &= (\cos t - i \sin t \frac{\mathbf{d}(\mathbf{k}) \cdot \boldsymbol{\sigma}}{d(\mathbf{k})}) |\psi(\mathbf{k}, 0)\rangle, \end{aligned} \quad (\text{S2})$$

then

$$\begin{aligned} \mathbf{P}(\mathbf{k}, t) &= \langle \psi(\mathbf{k}, 0) | (\cos t + i \sin t \frac{\mathbf{d}(\mathbf{k}) \cdot \boldsymbol{\sigma}}{d(\mathbf{k})}) \boldsymbol{\sigma} (\cos t - i \sin t \frac{\mathbf{d}(\mathbf{k}) \cdot \boldsymbol{\sigma}}{d(\mathbf{k})}) | \psi(\mathbf{k}, 0) \rangle \\ &= \cos^2 t \langle \psi(\mathbf{k}, 0) | \boldsymbol{\sigma} | \psi(\mathbf{k}, 0) \rangle + \sin^2 t \langle \psi(\mathbf{k}, 0) | \frac{\mathbf{d}(\mathbf{k}) \cdot \boldsymbol{\sigma}}{d(\mathbf{k})} \boldsymbol{\sigma} \frac{\mathbf{d}(\mathbf{k}) \cdot \boldsymbol{\sigma}}{d(\mathbf{k})} | \psi(\mathbf{k}, 0) \rangle \\ &\quad + i \cos t \sin t \langle \psi(\mathbf{k}, 0) | [\frac{\mathbf{d}(\mathbf{k}) \cdot \boldsymbol{\sigma}}{d(\mathbf{k})}, \boldsymbol{\sigma}] | \psi(\mathbf{k}, 0) \rangle. \end{aligned} \quad (\text{S3})$$

The expression for time-averaged pseudo-spin polarization in Eq.(4) of the main text is obtained by

$$\begin{aligned} \mathbf{P}(\mathbf{k}) &= \frac{1}{T} \int_0^T \mathbf{P}(\mathbf{k}, t) dt \\ &= \frac{1}{2} \langle \psi(\mathbf{k}, 0) | \boldsymbol{\sigma} | \psi(\mathbf{k}, 0) \rangle + \frac{1}{2} \langle \psi(\mathbf{k}, 0) | \frac{\mathbf{d}(\mathbf{k}) \cdot \boldsymbol{\sigma}}{d(\mathbf{k})} \boldsymbol{\sigma} \frac{\mathbf{d}(\mathbf{k}) \cdot \boldsymbol{\sigma}}{d(\mathbf{k})} | \psi(\mathbf{k}, 0) \rangle. \end{aligned} \quad (\text{S4})$$

By using $\langle \psi(\mathbf{k}, 0) | \sigma_z | \psi(\mathbf{k}, 0) \rangle = -1$ and $\langle \psi(\mathbf{k}, 0) | \sigma_{x,y} | \psi(\mathbf{k}, 0) \rangle = 0$, a further step leads to the final expression

$$P_i(\mathbf{k}) = -\frac{d_i(\mathbf{k})d_z(\mathbf{k})}{d_x^2(\mathbf{k}) + d_y^2(\mathbf{k}) + d_z^2(\mathbf{k})}. \quad (\text{S5})$$

II. PHASE DIAGRAM

Here we provide the details about the determination of the λ - μ phase diagram. Considering $\lambda_1 = \lambda_2 = \lambda$, the three components of the \mathbf{d} vector are given by

$$\begin{aligned} d_x(\mathbf{k}) &= 2\lambda(\sin k_x + \sin k_y) + \sin 2k_x + \sin 2k_y, \\ d_y(\mathbf{k}) &= 2\lambda(\sin k_y - \sin k_x) + 2\sin(k_y - k_x), \\ d_z(\mathbf{k}) &= 2\lambda(\cos k_x + \cos k_y) + \cos 2k_x + \cos 2k_y - \mu, \end{aligned} \quad (\text{S6})$$

For this Hamiltonian, the change of first-order topology is associated with the change of the parity of the Fermi surface (FS) number. One can readily find that it takes place at the two time-reversal momenta, $(0, 0)$ and (π, π) . Therefore, there are two critical μ for the topological phase transitions between first-order topological phases and other phases. The critical μ should lead d_z to satisfy $d_z(0, 0) = 0$ or $d_z(\pi, \pi) = 0$. Accordingly, we find

$$\mu_{c,1} = 4\lambda + 2, \quad \mu_{c,2} = -4\lambda + 2. \quad (\text{S7})$$

As there is only one FS when $\mu \in (-4|\lambda| + 2, 4|\lambda| + 2)$, the regime $(-4|\lambda| + 2, 4|\lambda| + 2)$ corresponds to the first-order topological superconducting phase.

When the parity of the FS number is even and one of the FS crosses the four removable Dirac pairing nodes (symmetry enforces that the crossing takes place simultaneously for the four removable Dirac pairing nodes), the system undergoes a topological phase transition between second-order topological superconducting phases and other phases. As $\Delta(\mathbf{k}) = d_x(\mathbf{k}) - id_y(\mathbf{k}) = 2[(\cos k_x + \lambda) + i(\cos k_y + \lambda)](\sin k_x - i \sin k_y)$, it is readily found that the four removable Dirac pairing nodes are located at $(k_{x;\pm}, k_{y;\pm}) = (\pm(\pi - \arccos \lambda), \pm(\pi - \arccos \lambda))$. At these four momenta, $d_z(k_{x;\pm}, k_{y;\pm}) = -2 - \mu$, and we obtain another critical value for μ when $|\lambda| < 1$, which is

$$\mu_{c,3} = -2. \quad (\text{S8})$$

The three phase boundaries divide the phase diagram into three topologically distinct regimes, as shown in Fig. S1.

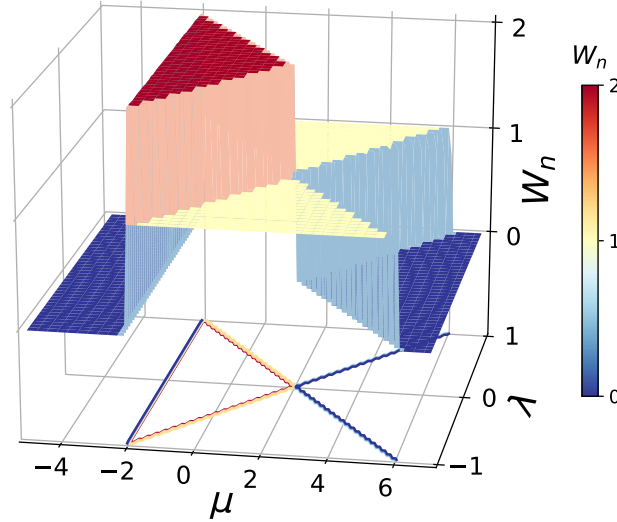


FIG. S1. The calculated winding number \mathcal{W}_n with varying λ and μ .

Let us now focus on the two high symmetry lines with $k_x = \pm k_y$, on which the Hamiltonian is reduced to

$$\begin{aligned} H(k_+) &= d_x(k_+)\sigma_x + d_z(k_+)\sigma_z, \\ H(k_-) &= d_y(k_-)\sigma_y + d_z(k_-)\sigma_z, \end{aligned} \quad (\text{S9})$$

where $k_{+(-)}$ represents the momentum on the line $k_x = (-)k_y$. As $\{H(k_+), \sigma_y\} = 0$ and $\{H(k_-), \sigma_x\} = 0$, the two reduced Hamiltonians both have chiral symmetry so their topological properties are characterized by the winding number, which can be written down compactly as

$$\mathcal{W}_{n;\pm} = \frac{1}{4\pi i} \int_{-\pi}^{\pi} \text{Tr}[C_{\pm} H^{-1}(k_{\pm}) \frac{\partial}{\partial k_{\pm}} H(k_{\pm})] dk_{\pm}, \quad (\text{S10})$$

where $C_+ = \sigma_y$ and $C_- = \sigma_x$ represent the respective chiral operators. If in terms of the \mathbf{d} vector, we have

$$\begin{aligned} \mathcal{W}_{n;+} &= \frac{1}{2\pi} \int_{-\pi}^{\pi} \frac{d_z \partial_{k_+} d_x - d_x \partial_{k_+} d_z}{d_x^2 + d_z^2} dk_+, \\ \mathcal{W}_{n;-} &= \frac{1}{2\pi} \int_{-\pi}^{\pi} \frac{d_y \partial_{k_-} d_z - d_z \partial_{k_-} d_y}{d_y^2 + d_z^2} dk_-. \end{aligned} \quad (\text{S11})$$

Depending on the choice $k_- = k_x = -k_y$ or $k_- = k_y = -k_x$, we have either $\mathcal{W}_{n;+} = \mathcal{W}_{n;-}$ or $\mathcal{W}_{n;+} = -\mathcal{W}_{n;-}$. As only the absolute value of winding number does not depend on the choice, throughout the whole paper, we only care about the absolute

value. A simple numerical calculation reveals that $\mathcal{W}_{n;\pm} = 1$ for the first-order topological superconducting phase, $\mathcal{W}_{n;\pm} = 2$ for the second-order topological superconducting phase, and $\mathcal{W}_{n;\pm} = 0$ for the trivial superconducting phase, suggesting that the winding number can fully distinguish all phases from each other.

III. PSEUDO-SPIN POLARIZATION DETERMINED IN EXPERIMENT

To demonstrate that quantum state tomography (QST) can faithfully determine the spin polarization, in this part we show the spin polarizations measured in experiment and those predicted according to the theoretical model together for comparison. For the sake of concreteness, we consider a sudden quench from $\lambda \rightarrow \infty$ (trivial) to $\lambda = -0.5$ and $\mu = -1.5$ (second-order TSC) and focus on the pseudo-spin polarization on the high symmetry line $k_x = k_y$, on which $d_y = 0$ and so the y -component of the time-averaged pseudo-spin polarization is zero. As we are only interested in the time-averaged pseudo-spin polarization, in this part we will only show the evolution of $P_x(\mathbf{k}, t)$ and $P_z(\mathbf{k}, t)$ whose time average are expected to be nonzero. Fig.S2(a)(b) show the evolution of the x - and z -components of the pseudo-spin polarization with time predicted by theory, and Fig.S2(c)(d) show the respective evolutions measured by QST. It is readily seen that the experimental results agree very well with the predicted values. Fig.S2(c)(d) also confirm the periodic behavior of pseudo-spin polarization.

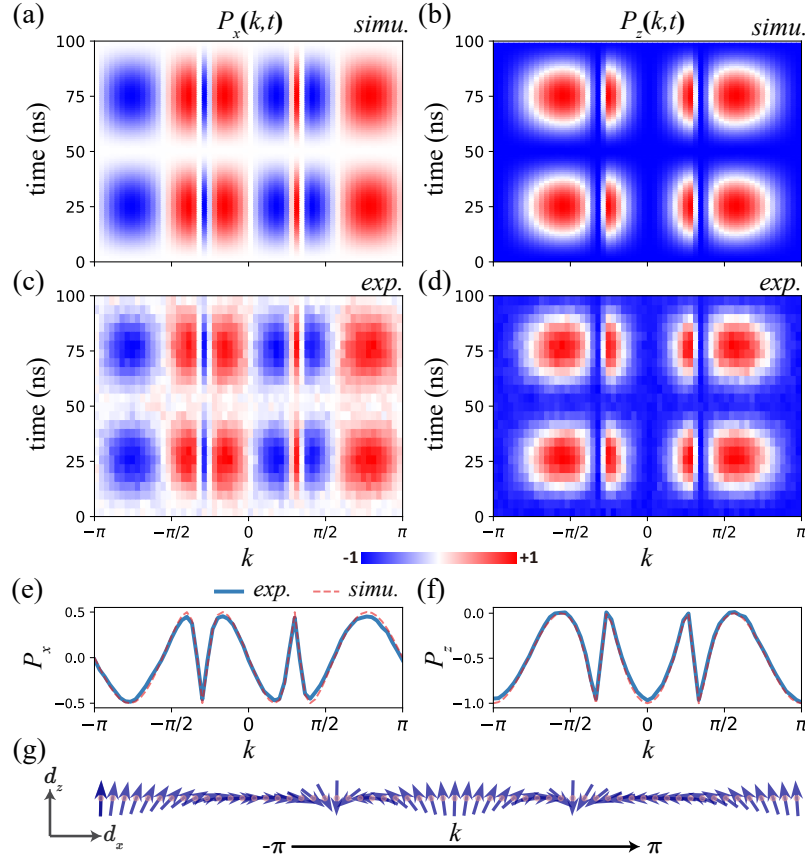


FIG. S2. Time-evolution of the pseudo-spin polarization $P_{x,z}(\mathbf{k}, t)$, for a typical example of $\lambda = -0.5$, $\mu = -1.5$. The numerical and experimental results are displayed in (a)(b) and (c)(d), respectively. (e-f) The corresponding time averaged pseudo-spin polarization $P_{x,z}$. (g) The two-component vector (d_x, d_z) along $k_x = k_y = k$ line experimentally deduced from (e-f).

According to the measured experimental data, we present the time-averaged pseudo-spin polarization in Fig.S2(e)(f). d_x and d_z can then be extracted from the experimental results in Fig.S2(e)(f). Fig.S2(g) shows the winding behavior of the two-component vector (d_x, d_z) across the Brillouin zone. It is easy to see that the two-component vector undergoes two complete cycles of winding when k goes from $-\pi$ and π , suggesting $\mathcal{W}_n = 2$ and so the realization of the second-order topological superconducting phase.

IV. REMOVABLE DIRAC PAIRING NODES AND TOPOLOGICAL PHASE TRANSITIONS BETWEEN SECOND-ORDER TSCS AND TRIVIAL SUPERCONDUCTORS

In this part, we provide more experimental data for the case with $\mu = -\lambda_1^2 - \lambda_2^2$. As mentioned in the main text, because of the constrain from the Hopf map, this case has only two topologically distinct phases, the second-order topological superconducting phase for $|\lambda_{1,2}| < 1$, and the trivial superconducting phase otherwise.

Focusing on $\lambda_1 = \lambda_2 = \lambda$, we tune λ from -1.2 to 1.2 . In Fig. S3, (a1)-(i1) on the left panel show the evolution of P_z , and (a2)-(i2) on the right panel show the evolution of (P_x, P_y) . It is readily seen that when λ goes across $\lambda_{c,l} = -1$ from below, two vortices and two antivortices emerge. With the further increase of λ , their positions move away from the time-reversal invariant momentum $(0, 0)$ in a symmetric way, while keeping located between the two contours for $P_z = 0$. When λ reaches $\lambda_{c,u} = 1$, the four movable vortices and antivortices coincide at the time-reversal invariant momentum (π, π) and then annihilate with each other. At $\lambda = \pm 1$, it seems that there is only one contour satisfying $P_z = 0$ (see (b1) and (h1)). In fact, this corresponds to the critical situation for which one of the contour is shrunk to a zero-size point (the time-reversal invariant momentum $(0, 0)$ for $\lambda = -1$ and (π, π) for $\lambda = 1$).

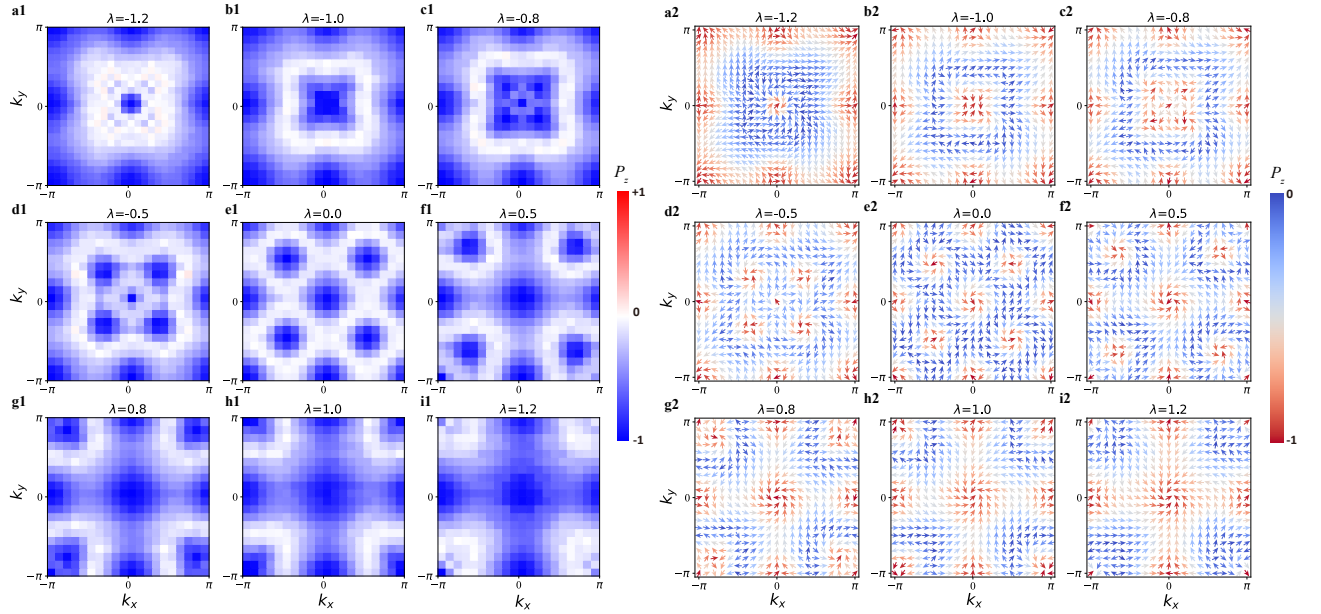


FIG. S3. λ -dependent removable Dirac pairing nodes and FS. (a)-(i) The FS (left) and pseudo-spin textures (right) displayed by P_z and (P_x, P_y) , respectively, for a wide range of λ from $\lambda < -1$ to $\lambda > 1$.

In Fig. S4, we show the pseudo-spin texture on the high symmetry line $k_x = -k_y$. As d_x vanishes on this line, the winding number is determined by the structure of (d_y, d_z) . As expected, the winding number is found to be $\mathcal{W}_n = 2$ in the regime $-1 < \lambda < 1$, and $\mathcal{W}_n = 0$ when $\lambda < -1$ or $\lambda > 1$, suggesting that the presence of removable vortices (or say Dirac pairing nodes) is crucial for the realization of second-order topological superconducting phase.

V. THE CHANGE OF PSEUDO-SPIN TEXTURE ACROSS TOPOLOGICAL PHASE TRANSITIONS

In this part, we provide a better view of the change of pseudo-spin texture across topological phase transitions. Here we still consider the case discussed in the main text. That is $\lambda = -0.5$. For this case, the critical points correspond to $\mu = -2, 0$ (that is $4\lambda + 2$), 4 (that is $-4\lambda + 2$). The pseudo-spin textures near these three critical points are presented in Fig. S5. From the results, it is readily found that when $\mu < -2$, the two-component vector (d_x, d_z) does not wind a complete cycle when k ($k = k_x = k_y$) goes from $-\pi$ to π , suggesting $\mathcal{W}_n = 0$; when $-2 < \mu < 0$, the two-component vector (d_x, d_z) is found to be able to wind the cycle completely when k goes from $-\pi$ to π , and the time of complete-cycle winding is found to be 2, suggesting $\mathcal{W}_n = 2$; when $0 < \mu < 4$, the two-component vector (d_x, d_z) is also found to be able to wind the cycle completely, but the time of complete-cycle winding is changed to 1, suggesting $\mathcal{W}_n = 1$; when $\mu > 4$, again the two-component vector (d_x, d_z) does not wind a complete cycle, suggesting that the system returns the trivial superconducting phase with $\mathcal{W}_n = 0$.

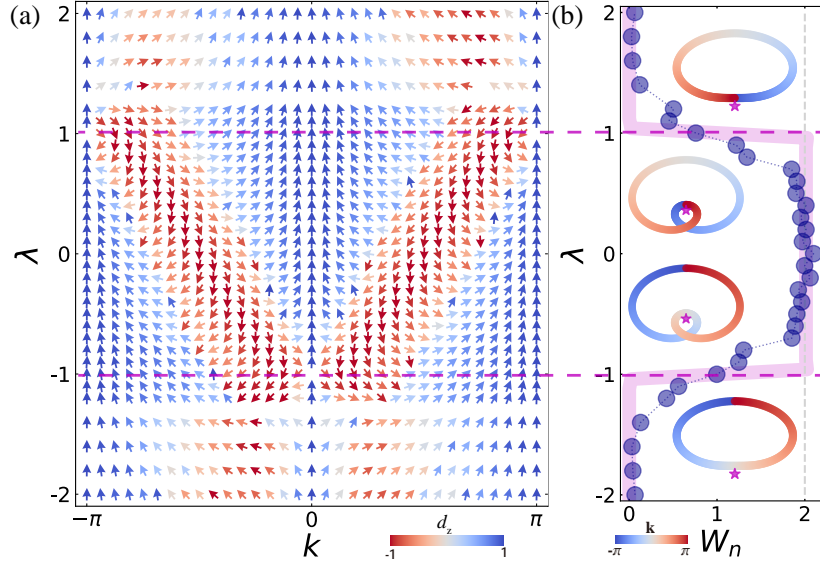


FIG. S4. Pseudo-spin texture (d_y, d_z) (a) and deduced winding number \mathcal{W}_n (b) along $k_x = -k_y$ line.

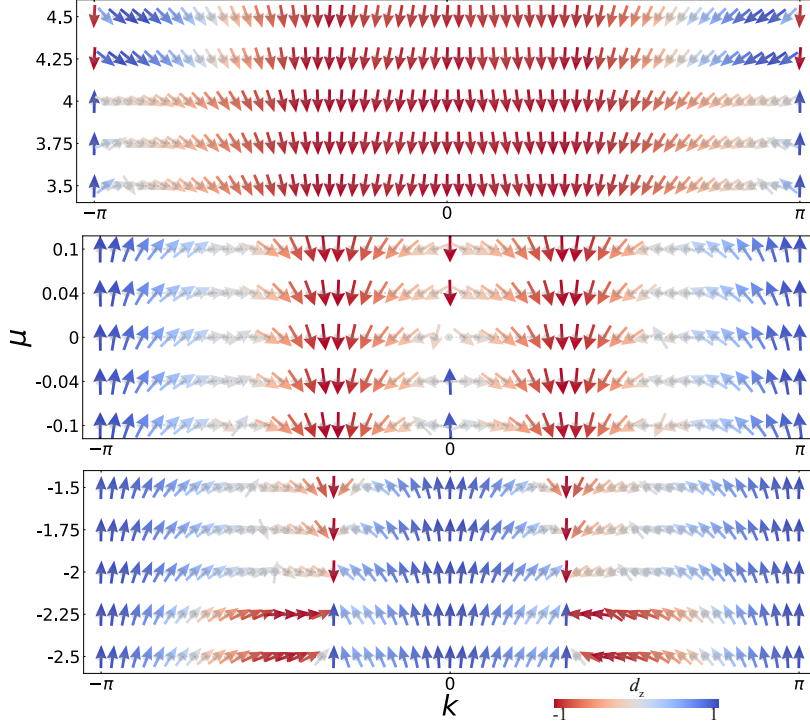


FIG. S5. A detailed display of (d_x, d_z) near the phase transition boundaries around $\mu = -2, 0, 4$ respectively.

VI. INFORMATION OF SAMPLES AND EXPERIMENTAL SETUP

Figure S6 shows the optical image of our Xmon qubit for experiments. The microwave pulse, with amplitude Ω and frequency $\omega_d = \omega_{01} + \delta$ (δ is detuning), is applied to the qubit through the XY-drive line, and the qubit frequency is tuned through the Z-control line. A $\lambda/4$ resonator (its frequency is $\omega_r/2\pi = 6.8308$ GHz) is dispersively coupled to the Xmon qubit for readout, and the state of the qubit can be deduced by measuring the transmission coefficient S_{21} of the transmission line [S1–S3].

We would like to note that all data except for Fig. S4 presented in this work were obtained from one superconducting Xmon qubit. The qubit frequency is $f_{10} = \omega_{01}/2\pi = 5.04$ GHz, and the relaxation and dephasing times at this frequency are

$T_1 = 17.48 \mu\text{s}$ and $T_2 = 0.82 \mu\text{s}$ for the first excited state, respectively. While the data for Fig. S4 were acquired from another qubit, with qubit parameters $f_{10} = \omega_{01}/2\pi = 5.908 \text{ GHz}$, $T_1 = 3.81 \mu\text{s}$ and $T_2 = 1.84 \mu\text{s}$.

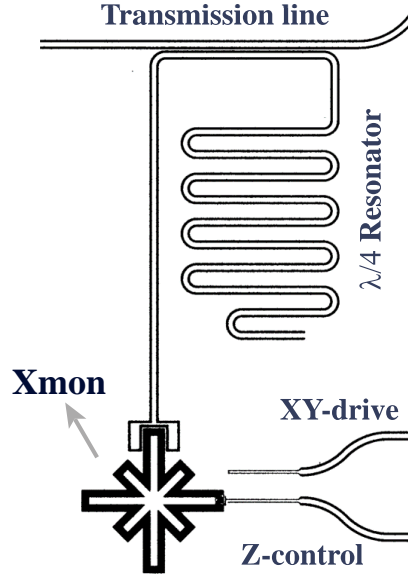


FIG. S6. The optical image of the Xmon qubit used in our experiment.

* These authors contributed equally to this work.

† lius3@sustech.edu.cn

‡ yanzhib5@mail.sysu.edu.cn

§ chenyz@sustech.edu.cn

- [S1] R. Barends, J. Kelly, A. Megrant, A. Veitia, D. Sank, E. Jeffrey, T. C. White, J. Mutus, A. G. Fowler, B. Campbell, Y. Chen, Z. Chen, B. Chiaro, A. Dunsworth, C. Neill, P. O'Malley, P. Roushan, A. Vainsencher, J. Wenner, A. N. Korotkov, A. N. Cleland, and J. M. Martinis, *Nature* **508**, 500 (2014).
- [S2] M. D. Reed, L. DiCarlo, B. R. Johnson, L. Sun, D. I. Schuster, L. Frunzio, and R. J. Schoelkopf, *Phys. Rev. Lett.* **105**, 173601 (2010).
- [S3] D. Sank, Z. Chen, M. Khezri, J. Kelly, R. Barends, B. Campbell, Y. Chen, B. Chiaro, A. Dunsworth, A. Fowler, E. Jeffrey, E. Lucero, A. Megrant, J. Mutus, M. Neeley, C. Neill, P. J. J. O'Malley, C. Quintana, P. Roushan, A. Vainsencher, T. White, J. Wenner, A. N. Korotkov, and J. M. Martinis, *Phys. Rev. Lett.* **117**, 190503 (2016).